A High Precision Initial Position Estimation Method for Low Saliency Ratio Machine Based on Image Tracking

Henghong Wang, *Student Member, IEEE*, Jiyao Wang, *Member, IEEE*, and Wei Xu, *Member, IEEE*

***Abstract*—In sensorless control of permanent magnet synchronous motor drives, initial rotor position detection is critical to ensure smooth start-up operation. However, extracting initial position information for machines with ultra-low saliency ratios is challenging. To address this issue, this article proposes an estimation method for rotor position using image tracking based on high-frequency rotating voltage vector injection. Specifically, this article extracts positive- and negative-sequence currents in the stationary reference frame and reconstructs the induced current vector. By utilizing the support vector machine algorithm, the resulting current vector images, which contain amplitude and phase information of the position, are trained to establish the correlation between the current image and rotor position information. Ultimately, the electric position can be obtained from image recognition. Since this method employs image tracking for position estimation, it accounts for cross-saturation and multiple saliencies, leading to the relatively high precision of position estimation. Experimental evaluation shows that the proposed method achieves higher precision compared to conventional observers.**

***Index Terms*—High-frequency (HF) injection, magnetic polarity, sensorless control, support vector machine (SVM).**

NOMENCLATURE

i_d, i_q	$d-$ and $q-$ axis components of stator current in the synchronous reference frame, respectively.
i^s_{dh}, i^s_{qh}	High-frequency stator $d-$ and $q-$ axis current vector in the stator reference frame.
i^s_c	High-frequency current vector in a stationary reference frame.
i^r_c	High-frequency current vector in a synchronous reference frame.
i_a, i_b	Phase of a, b current.
$I_p,\ I_n$	Amplitude of the equivalent positive- and negative-sequence carrier currents.
i_{pn}	Reconstructs the induced current vector.
L_d, L_q	$d-$ and $q-$ axis stator self-inductances.
L_{qd}, L_{dq}	$d-$and $q-$ axis stator mutual inductances.
L_{dh}, L_{qh}	High-frequency $d-$ and $q-$ axis stator self-inductances.
L_{qdh},L_{dqh}	High-frequency $d-$ and $q-$axis stator mutual-inductances.
L_{sa}	Average inductance of $d-$ and $q-$ axis stator.
L_{sd}	Half difference inductance between $d-$ and $q-$ axis stator.
R_s	Armature winding resistance.
λ_{pm}	Permanent magnetic flux linkage.
P_n	Number of pole pairs.
J	Rotor inertia.
ω_e	Rotor speed at electrical angle.
ω_c	Speed of the rotating injected high-frequency voltage signal.
u_q,u_d	$d-$ and $q-$axis components of stator voltages in the synchronous reference frame.
u^s_c	High-frequency voltage vector in a stationary reference frame.
u^r_c	High-frequency voltage vector in a synchronous reference frame.
V_c	Amplitude the injected high-frequency rotating carrier voltage signal.
$\phi_{2p},\ \phi_{2n}$	Phase angle of the second positive- and negative-sequence current.
ϕ_h	Phase angle of the hth harmonic current.
θ_e	Actual electrical angle.
$\hat{\theta}_e$	Estimated electrical angle.
θ'_e	The previously estimated electrical angle.
p	Derivative operator.
w^{T}	Transposed matrix of the matrix w.
$\|\|$	Absolute-value operator sign.
$\int, 1/\text{s}$	Integral operator.
Re, Im	Real and imaginary part of the vector.
PID	Proportional–integral–differential controller.
K_P, K_I, K_D	Parameter of the proportion, integral, and differential of PID controller.
LSO	Luenberger style observer.
LUT	Look-up table.
GLCM	Gray level co-occurrence matrix.
HOG	Histogram of oriented gradient.

Manuscript received 18 April 2023; accepted 23 May 2023. Date of publication 29 May 2023; date of current version 22 September 2023. This work was supported in part by the National Natural Science Foundation of China under Grants 52037002, 52275009, and 52207038; and in part by the Fundamental Research Funds for the Central Universities under Grant 3216002209A1. Recommended for publication by Associate Editor A. Trzynadlowski. *(Corresponding author: Wei Xu.)*

The authors are with the School of Electrical Engineering, Southeast University, Nanjing 210096, China (e-mail: wanghh@seu.edu.cn; jyaowang@seu.edu.cn; weixu@seu.edu.cn).

Color versions of one or more figures in this article are available at https://doi.org/10.1109/TPEL.2023.3280939.

Digital Object Identifier 10.1109/TPEL.2023.3280939

I. Introduction

FIELD-ORIENTED vector control or direct torque control is usually used in the ac drive system because of the excellent precision and dynamic control of the speed and position domain. Nevertheless, precise information of the rotor position and speed is essential, measured directly by mechanical position sensors installed coaxially with the rotor. This not only leads to increases in the cost and size of the motor system but also degrades the reliability and stability of the system due to the additional wiring and connections to sensors. To solve these problems, sensorless control technology is proposed. It has been the industrial and academic research focus and an ongoing subject of investigation [1], [2], [3], [4], [5], [6].

In the field of sensorless control, there are two main categories: fundamental-model-based control and saliency-based control, as discussed in [5]. The former utilizes the back electromotive force (EMF) of permanent magnet synchronous motors (PMSMs) to estimate position. Still, it is only effective for the medium–high-speed range, as the amplitude of back-EMF is proportional to the speed [7], [8], [9], [10]. On the other hand, saliency-based sensorless control is adapted for the low-speed range, as it requires a minor EMF effect. Consequently, the high-frequency (HF) signal injection method based on saliency tracking can be used to obtain the initial rotor position. Multiple sinusoidal HF carrier signal injection methods have been proposed for position estimation, utilizing either rotating vector voltage injection [11], [12], [13], [14], [15], [16] or pulsating voltage vector injection [5], [6], [17], [18], [19], [20].

The prerequisite for accurate sensorless control is to estimate the initial rotor position precisely. However, extracting the initial position accurately is challenging, and misalignment during start-up can lead to motor failure or even reversal [6]. The commonly used initial position detection scheme involves pulling the rotor to a preset position before starting up [4], [6], [21], [22], [23]. Nonetheless, in certain critical applications, such as broaching, electric vehicles, and elevators, rotor fluctuations are prohibited during start-up.

Saliency is indispensable when using the method of HF injection-based sensorless control [24]. For surface permanent magnet synchronous motors (SPMSMs), which have no or poor saliency, position information is extracted using saliency that depends on the magnetic saturation on the leakage flux paths. However, cross-saturation and slotting effects can significantly affect saturation saliency [4], [25]. Compared with HF rotating signal injection, HF pulsating voltage injection offers higher accuracy of rotor position estimation for machine with low saliency [5], while the system may be unstable due to the ambiguous convergent point [26].

In the aforementioned HF injection methods, a low-pass filter (LPF) is necessary to extract the position signal. However, this leads to a decrease in system bandwidths, introduces additional phase lag. In addition, various factors, such as dead bands for power switches, nonideal behavior of inverters, stator and rotor resistances, and cross-saturation, can create angular offsets or mean estimation errors for position estimation [27]. To improve the accuracy of observer, several approaches are investigated, such as offline experimental [16], [18], estimation on d-, q-inductance online [21], [22], and tracking multiple spatial harmonic saliencies [11], [13]. However, the overall estimation accuracy using traditional observers based on without any compensation is unsatisfactory. Undesirable saliencies can cause errors or complete failure of the HF injection method, especially for motors with very small anisotropies. To address this issue, a compensation method utilizing current vector angle adaptive adjustment online for estimated rotor position has been proposed in [28]. In [29], an initial position estimation method was proposed based on the dynamic equation of a PMSM to address the limitations of low adaptability to PMSMs with varying saliency and high sensitivity to electrical parameters. However, the method requires an additional vibration sensor, resulting in increased costs and reduced reliability. In contrast, in Xu and Zhu [30], a method utilized zero-sequence carrier voltage for initial rotor position estimation so as to achieve a large signal-to-noise ratio (SNR) and excellent stability for sensorless control. However, this approach requires one balanced resistor network and hardware setup for voltage sensing, which increases system size and degrades overall reliability.

To avoid decreasing system bandwidths, HF square wave injection is utilized instead of HF sinusoidal injection in [31], while there are multiple convergent points and position errors in HF square wave injection. Another technique proposed in [6] involves adding a virtual HF rotation frame based on traditional HF pulsating injection without requiring PI regulation.

Although initial position can be obtained using the aforementioned methods, they strongly depend on the predefined inductance model and suffer from electromagnetic interference (EMI). In order to reduce the impact of noise generated by single-frequency, the estimated initial position can be obtained by analyzing the time required for the charging current to reach its peak value in the bootstrap circuit [23]. However, this method is limited by errors caused by unbalanced magnetic fields and nonlinearity of inductance. In [26], another approach is proposed which compares the amplitudes of the three-phase HF currents to mitigate the effect of noise. Nevertheless, this method has a 30° estimation resolution as it relies on rotor sector detection. For higher SNR, transient short pulse injection [8], [9], [10], [11], [12] has robust and reliable identification performance but leads to slower convergence since it needs additional signals to change the magnetic saturation as the next step.

Previous literatures in the field of position estimation for PMSMs have relied primarily on phase or magnitude scalar methods. However, these methods are vulnerable to distortion by undesired saliency signals, leading to lower accuracy of position estimation. To overcome this issue, a position estimation method based on image-tracking was proposed in [32]. This method uses the correlation value between the template image and test image to determine the estimated rotor position. While using only one correlation value as an image feature for image tracking, it is still challenging to achieve high precision position estimation. Additionally, the template images do not include polarity information, dictating an additional rotation operation for polarity identification.

In contrast, our proposed method utilizes the current image in the stationary reference, which includes polarity information, to directly establish correlation between the current vector image and rotor position information through support vector machine (SVM). The SVM has the ability to obtain rich image features, which enables accurate image tracking. Experimental results demonstrate that the proposed method is capable of achieving good position estimation performance for low saliency machine, even in the presence of interference. In conclusion, the proposed method provides a promising approach toward more accurate sensorless control for PMSMs with low saliency.

The rest of this article is organized as follows. Section II, an overview of the HF voltage injection method, focuses on the current vector image and introduction of the SVM algorithm. Section III describes the complete process of access to position information using image identification. In Section IV, the experiments are conducted at various injection positions, and the performance of rotor position estimation is experimentally evaluated and discussed. Finally, Section V concludes this article.

II. Track of HFI Current

A. HFI Mathematical Model of PMSM

The stator voltage model for a PMSM can be represented as follows in the synchronous reference frame:

$$\begin{bmatrix} u_q \\ u_d \end{bmatrix} = \begin{bmatrix} R_s & 0 \\ 0 & R_s \end{bmatrix} \begin{bmatrix} i_q \\ i_d \end{bmatrix} + \begin{bmatrix} L_q & L_{dq} \\ L_{qd} & L_d \end{bmatrix} p \begin{bmatrix} i_q \\ i_d \end{bmatrix} + \begin{bmatrix} \lambda_{\text{pm}}\omega_e \\ 0 \end{bmatrix}. \quad (1)$$

When injecting an HF signal, the resistive voltage drop becomes less significant than the induced voltage, and the EMF can be ignored at low speeds. Thus, the stator HF voltage equations can be approximated as

$$\begin{bmatrix} u_{qh} \\ u_{dh} \end{bmatrix} = \begin{bmatrix} L_{dh} & L_{dqh} \\ L_{qdh} & L_{qh} \end{bmatrix} p \begin{bmatrix} i_{qh} \\ i_{dh} \end{bmatrix}. \quad (2)$$

To obtain the rotor position information, a balanced three-phase HF voltage with constant carrier frequency is injected into the fundamental component voltage vector of the motor

$$u_c^s = V_c \ e^{\text{j}\omega_c t} = V_c \ (\cos\omega_c t + \text{j}\sin\omega_c t). \quad (3)$$

Transforming this (3) into the synchronous frame reference

$$u_c^r = V_c \, e^{\text{j}\omega_c t} \, e^{-\text{j}\theta_e} = V_c \, e^{\text{j}(\omega_c t - \theta_e)}. \quad (4)$$

By substituting (2) into (4) followed by mathematical transforms, the HF current response can be shown as follows:

$$i_c^r = \frac{V_c}{L_d} \int \cos(\omega_c t - \theta_e)\,\text{d}t + \text{j}\frac{V_c}{L_q} \int \sin(\omega_c t - \theta_e)\,\text{d}t. \quad (5)$$

Transform (5) into the stationary frame reference

$$i_c^s = i_c^r \ e^{\text{j}\theta_e} = I_p \, e^{j\left(\omega_c t - \frac{\pi}{2}\right)} + I_n e^{j\left(-\omega_c t + 2\theta_e + \frac{\pi}{2}\right)} \quad (6)$$

TABLE I
Explanation of Symbol in (8)

Symbol	Explanation
I_{c_p1}	The amplitude of the positive-sequence current induced by the primary saliency.
I_{c_n1}	The amplitude of the negative-sequence current induced by the primary saliency.
I_{c_p2}	The amplitude of the positive-sequence current induced by the second-order saliency.
I_{c_n2}	The amplitude of the negative-sequence current induced by the second-order saliency.
I_{c_nh}	The amplitude of the negative-sequence current induced by the h-order saliency.

where I_p and I_n represent the amplitudes of the equivalent positive- and negative-sequence carrier currents, respectively

$$I_p = \frac{V_c}{\omega_c}\left(\frac{L_{sa}}{L_{sa}^2 - L_{sd}^2}\right);\ I_n = \frac{V_c}{\omega_c}\left(\frac{L_{sd}}{L_{sa}^2 - L_{sd}^2}\right). \quad (7)$$

When considering magnetic saturation and secondary saliencies, the current response can be modeled by (8). In this equation, I_{c_nh} represents the amplitude of the negative sequence current induced by the hth order saliency. Regardless of whether or not secondary saliencies are considered, position information can still be extracted from the negative sequence of the current response, as demonstrated in [12] and [13]

$$\begin{aligned} i_{dqc}^s \approx\ & I_{c\_p1} e^{j\left(\omega_c t - \frac{\pi}{2}\right)} + I_{c\_n1} e^{j\left(-\omega_c t + 2\theta_e + \frac{\pi}{2}\right)} \\ & + I_{c\_p2} e^{j(2\omega_c t - \theta_e + \phi_{2p})} + I_{c\_n2} e^{j(-2\omega_c t + 3\theta_e + \phi_{2n})} \\ & + j\sum I_{c\_nh} e^{j(-\omega_c t + h\theta_e + \phi_h)}. \end{aligned} \quad (8)$$

The symbols used in (8) are explained in Table I. As seen from (8), even though multiple saliencies are considered, position information can still be obtained from the current in the stationary frame. There are four parts in (8) that contain spatial (rotor position) information. These parts include the carrier frequency of the negative sequence components, the second harmonic of the negative- and positive-sequence components, and the hth harmonic of the negative sequence components.

The carrier frequency of the negative-sequence components contains the twofold electrical rotor position ($2\theta_\text{e}$). The second harmonic of the negative- and the positive-sequence components include the fundamental element (θ_e) and the threefold of the electric rotor position ($3\theta_\text{e}$), respectively. Both the second harmonic of the negative- and the positive-sequence components include odd multiple rotor positions, which is why the second harmonic of current can be used to distinguish the magnetic polarity. Finally, the hth harmonic of the negative sequence components contains the h-fold of the electric rotor position ($h\theta_\text{e}$).

B. Tracking Observer Rotating HFI Model

The rotor position is necessary to transform the current from a stationary reference frame to a synchronous reference frame. However, before it can be estimated, the rotor position cannot be

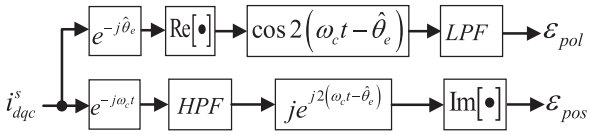

Fig. 1. Process to extract the information of the polarity and the position error.

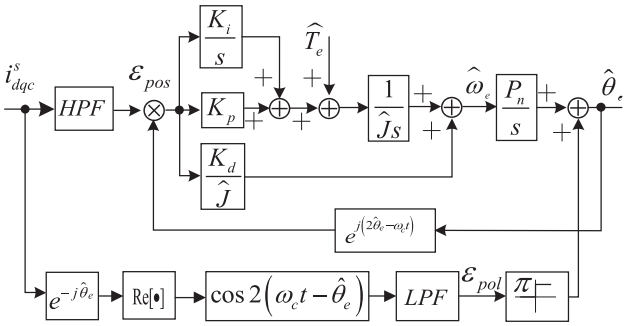

Fig. 2. Observer for rotor position estimation.

applied to sensorless control. The traditional observer method, based on HF rotating voltage injection, involves extracting the negative-sequence current using a synchronous frame filter (SSF) modulating the negative-sequence current with a heterodyne filtering technique to acquire the position error signal, and obtaining the estimated position with the aid of LSO. As previously mentioned, the negative-sequence term contains the position information, while the saturation term includes the magnetic polarity. Heterodyning and SSF are used to obtain the position error, as depicted in Fig. 1. However, to extract these signals, an HPF and an LPF are needed, which can introduce phase bias in sensorless control.

Commonly, an LSO is designed to estimate the position. The position error ε_{pos} is used as the input signal to LSO with torque command feedforward to obtain a position with zero phase lag. The illustrative diagram of LSO is as shown in Fig. 2.

In low saliency ratio conditions, secondary saliencies may have a greater magnitude than the primary saliency, which can attenuate estimation accuracy. To improve estimation performance and utilize the multipoles information fully, a sensorless control method based an image tracking is proposed.

C. Image-Tracking Rotating HFI Model

A vector signal is a graphical and pictorial description that provides more insight than scalar values representing magnitude or phase, as it contains both amplitude and phase information. Thus, it is more reliable to extract position information from current vectors rather than using amplitude or phase modulation alone [32]. According to (8), the current contains position information except for the carrier frequency of the positive-sequence term.

While any single vector presents a pure circle image in the real and imaginary expression, the circle's radius varies at different positions, which can make identifying the current image accurately difficult, particularly in cases with low saliency ratios. To obtain enough position features in the position variation of the

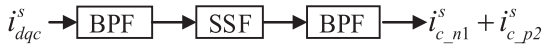

Fig. 3. Process of rebuilding vector.

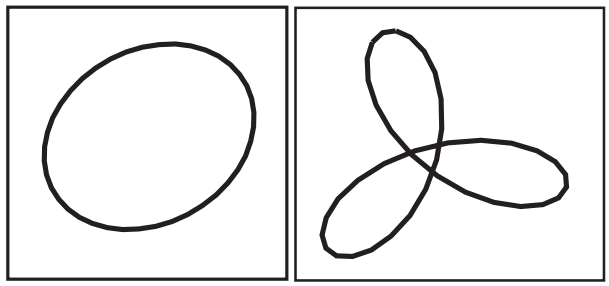

Fig. 4. Image of current vectors at a position. (a) Current trajectory in the synchronous reference frame. (b) Rebuilt current vector trajectory in the stationary frame.

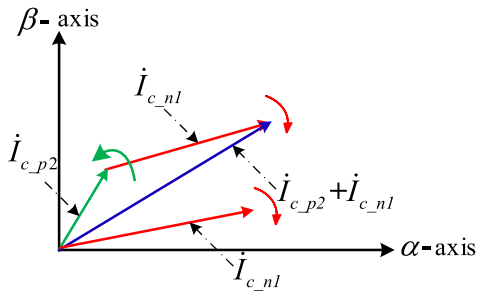

Fig. 5. Diagram of the rebuilt vector.

current vector, a composite current vector is rebuilt by employing the HF primary negative-sequence current superimposed on the second harmonic of the positive-sequence current, which can distinguish the magnetic polarity. The process of accessing the rebuilt vector is described in Fig. 3. When plotting the q-axis current along the x-axis and the d-axis along the y-axis, the current image over one injection period becomes an ellipse, as shown in Fig. 4(a).

This article proposes a different approach compared to [32], which detects rotor position by evaluating the orientation of the current image in a synchronous reference frame. In [32], the current image template is rotated by a small increment of one step to search for an angle that represents the estimated rotor position. This occurs only if the correlation value of the rotated template image and the test current image is the maximum in a cycle. When plotting the q-axis current along the x-axis and the d-axis along the y-axis, the current image over one injection period is an ellipse, as shown in Fig. 4(a).

According to (8), the HF current response can be divided into two components: the HF primary negative-sequence current response rotating counterclockwise at the speed ω_c, and the second harmonic positive-sequence current response rotating clockwise at speed $2\omega_c$. Fig. 5 shows a diagram of the rebuilt vector composed these two components.

To demonstrate the effect of load on the composite vector image, Fig. 6 shows the vector image at five different rotating

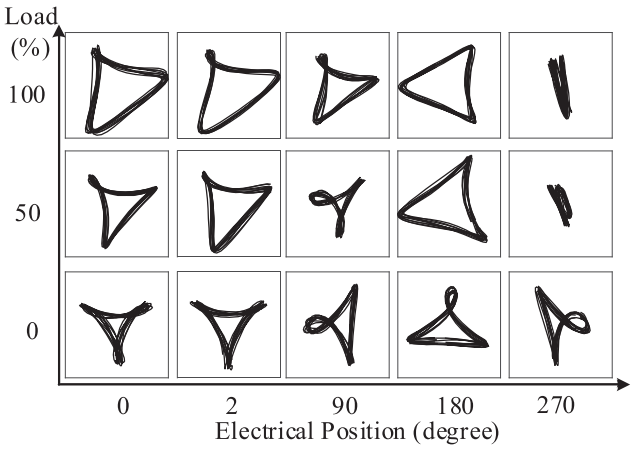

Fig. 6. Image of the rebuilt vector versus rotating injection angles with different load.

injection angles in SPMSM machines under three different load conditions: 0%, 50%, and 100%. It can be observed that each composite current image is unique, particularly when the injection angles change. This indicates that the composite current vector image contains position information and varies with the injection angles. By comparing the current track at various injection angles, it is apparent that the location and shape of the current images differ in the same sketching plane. These differences are essential for image recognition, which is why the composite current vector image can be utilized for position identification.

Furthermore, with an increase in fundamental currents, the profile of the individual composite current shape becomes more significant. This suggests a saliency variation in relation to the fundamental currents and is attributed to feature extraction. Consequently, this article establishes a correspondence between the current image and the rotor position information based on image recognition technology. This transformation enables the investigation of rotor position information to be converted into research on the identification of the current image.

D. Mathematical Model of SVM

SVM is a supervised machine-learning algorithm based on statistical learning theory and the structural risk minimization principle. Through kernel functions, SVM can transform a nonlinear separable problem into a linearly separable one in Hilbert space. SVM has shown excellent performance in solving small sample high-dimensional pattern classification. Moreover, it has good generalization, fast computation speed, and high accuracy. As a result, SVM has been utilized to forecast wind speed in [33] and [34]. Furthermore, SVM is used to predict flux linkage in [35]. In [36], SVM based on the ripple component is utilized for speed and position estimation of brushed dc motors.

The SVM algorithm maps the linearly separable training samples to the high-dimensional space at first and subsequently utilizes the maximization interval method to search the separation hyperplane. A separating hyperplane can be defined as the following equation: $w^{\mathrm{T}}x_i + b = 0$, where w is a decision

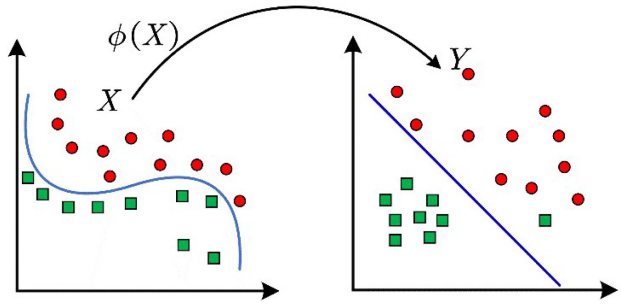

Fig. 7. Process of nonlinear transformation.

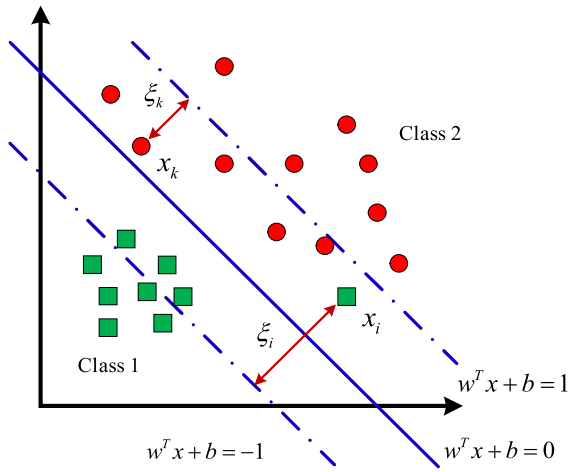

Fig. 8. Slack variables for linearly nonseparable data.

hyperplane normal vector and b is the intercept term to select the hyperplane, i.e., perpendicular to the normal vector. When the classes cannot be separated linearly, the samples need to be transformed into a high-dimensional space where they can be linearly separated. This transformation is achieved through a kernel function $\phi(x_i, x_j)$, which maps the data from the input space to a feature space where the classes become linearly separable. As Fig. 7 presents, the process of nonlinear transformation from input space high-dimensional feature space.

The kernel function used in this article is the Gaussian kernel function, with its expression shown as

$$\phi\ (x_i, x_j) = \exp\left(-\frac{\|x_i - x_j\|^2}{2\sigma^2}\right). \tag{9}$$

Assume there is an image set of K object categories$D = \{(x_1, y_1), (x_2, y_2), \ldots, (x_N, y_N)\}$, where$y_i \in (1, \ldots, \mathrm{K})$. To ensure all training instances satisfy the constraint of separating hyperplane, it is essential to introduce a slack variable $\xi_i \geq 0$ $(i = 1,2,\ldots,)$ for each training instance so that the value of geometric interval adds a slack variable is not less than 1. When training instance x_i is on or outside the correct interval boundary, as shown in Fig. 8. After introducing the slack variable and

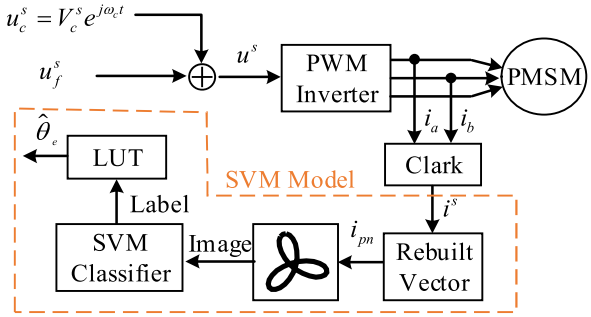

Fig. 9. Block diagram of the initial position process.

changing the constrain, the form of SVM can be written as

$$\begin{aligned} &\min_{w,b,\xi} \tfrac{1}{2}\|w\|^2 + C\sum_{i=1}^{N}\xi_i \\ &s.t.\, y_i(w^{\mathrm{T}}x_i + b) \geq 1 - \xi_i \\ &\xi_i \geq 0, i = 1, 2, \ldots, N \end{aligned} \tag{10}$$

where $C > 0$ is a normalization value used to determine the number of errors that can be tolerated in a training set. If the value of C is large, the penalty for misclassification will increase and vice versa. The constraint in (10) requires that all training examples can be correctly classified after introducing slack variables.ξ_i are slack variables and describe the extent to which the data do not satisfy the constraint $y_i(w^{\mathrm{T}}x_i + b) \geq 1$; x_i is the input feature vector; y_i are the associated output class label of x_i, and N is the set of features in each sample. The term $\frac{1}{2} \parallel w\parallel^2$ represents a structural risk, and it aims to reduce the complexity of the model or increase the classification interval as much as possible; the term $C\sum_{i=1}^{N}\xi_i$ indicates the empirical loss, which aims to reduce the number of misclassification instances or increase the fit between the model and training data to the most considerable possible extent, and the constant C is the compromise between the amount cost of misclassification instances in the training set and the complexity of the model.

III. Image Identification Modeling

A. Process of Image Identification

The block diagram shown in Fig. 9 illustrates the image-based initial position identification process using the SVM model. The system comprises an SVM classifier and a look-up table. As shown in Fig. 3, the process of current vector rebuilding is conducted to obtain the inputs and outputs of the SVM classifier, which are rebuilt current vector images and corresponding labels representing the rotor position, respectively. To simplify, a number of type double defined as a label corresponding to the rotor position. For example, 2 represents the 2° position. However, during actual testing, interference signals were present due to undesired signals. When the categorization label value is 362, the signals are recognized as interferences, and the program maintains the estimated position as the previously estimated value. To further clarify this process, Table II is included, which illustrates the relationship between the position and its corresponding label.

TABLE II
Corresponding Between Position and Labels

Label	0	2	4	.....	356	358	362
position	0	2	4	.....	356	358	$\theta_e^{'}$

And then, the SVM classifier is used to identify to current image from the current response at the injection position. The LUT is used to match the position angle according to the label.

A continuously rotating and balanced three-phase carrier HF voltage vector was superimposed onto the fundamental component voltage vector in the stationary reference frame. The current analog–digital conversion circuits measure the three-phase current containing both the fundamental and HF components. Finally, the rotor angle is achieved with appropriate signal processing, as mentioned above.

Based on (8), the rebuilt current vector consists of the real and imaginary parts. In order to eliminate the error of the stator current, the buffer size is determined to ensure the convergence of 10 cycles of the HF current waveform according to the sampling frequency of the current.

The current image is plotted to employ the real part along the x-axis and the imaginary part along the y-axis. Then, the current image is fed to the trained SVM classifier. After the current image is identified and labeled, the estimation position angle can be acquired.

In order to train the SVM classifier model, we need the encoder as a reference for training the parameters. To ensure the accuracy of the training model, the rotor is locked to the injection angle during the injection progress. Then, the responding current image is obtained at series rotor positions.

B. Image Identification Model Using SVM

To train a multicategory classification for the identification of a current image, four processes are involved: image preprocessing, feature extraction, identification classification, and matching of the current image. The acquisition and feature extraction of the current image data are explained below. Additionally, this article explains the techniques required for each step in multicategory classification, as shown in the flowchart in Fig. 10.

Step 1 Define the number of categorizations.

The number of categorizations must be carefully chosen because it directly correlates with the position precision. A larger number of categorizations can provide greater precision, but it also results in a relatively large model and longer computation time. To achieve a better tradeoff between overall accuracy and consumption of time for position estimation, this article selected 180 position categorizations, dividing an electrical cycle into 180 equal parts, with parts of two electrical degrees at each interval considered as a categorization label. An additional classification was added to recognize dynamic interference signals, improving the recognition rate in dynamic cases. Therefore, 181 categorizations were selected for this article.

Step 2 Obtain the data of the train and test.

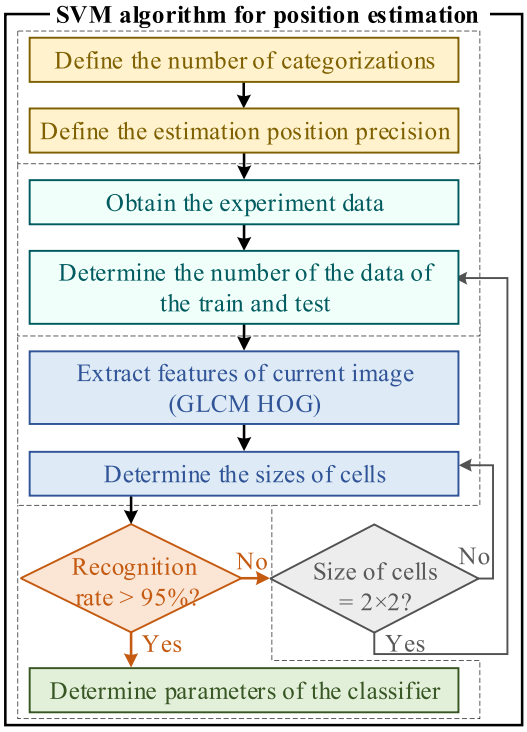

Fig. 10. SVM algorithm for position estimation.

A total of 50 experiments were conducted at each position to obtain 9000 samples from the experiment results, considering nonlinear effects, such as nonideal behavior of the inverter and sensor resolution. It is noted that the interference image data were manually selected from the experimental image data. To remove experimental errors, 10 multiplied periods of carrier frequency were included in every experiment at each position. Thirty-eight data groups were randomly selected to train the SVM for nonlinear mapping between position information and current image. To verify the model in every position, the remaining 12 groups of data were used as the test sets.

Step 3 Extract features of the current image.

Feature extraction is the process of simplifying an image by extracting valuable information and discarding irrelevant information. Extracting eigenvectors is a crucial step in image identification, and can be achieved using methods, such as edge detection, histogram analysis, texture analysis, and shape analysis. In this article, the HOG method of edge detection is employed because an edge-detected image contains valuable feature information. The GLCM method is also utilized, as it effectively captures comprehensive information about the direction, adjacent interval, and changing amplitude of a grey-level image. Features derived from HOG and GLCM are then fed into an SVM to identify defects classification.

To avoid a sparse feature extraction that would result in a heavy computational burden with potentially lower identification precision, the whole image is divided into several 4×4 small cells. By calculating the HOG of each cell, more compact features are represented. To describe the local variation characteristics of the image in horizontal, vertical, and diagonal directions, GLCMs in four directions of 0°, 45°, 90°, and 135° are selected. Characteristics, such as energy, contrast, correlation, and homogeneity, are chosen to describe the texture feature of the image. The entire feature extraction process from the current image is presented in Fig. 11.

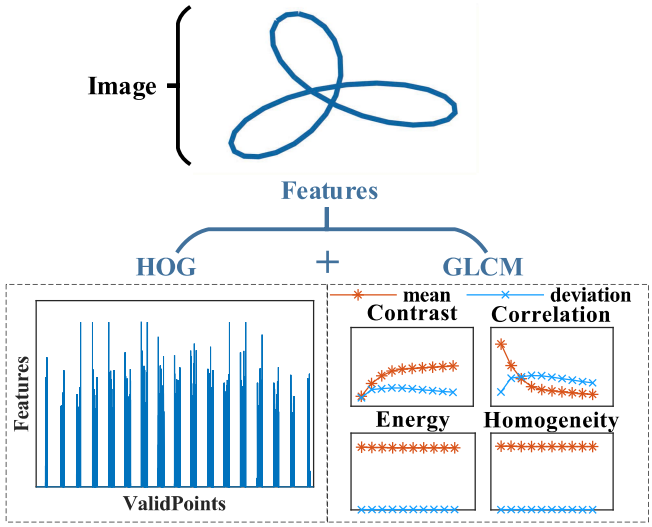

Fig. 11. Extract features of the current image.

Step 4 Evaluate the model of position estimation.

The accuracy of the confusion matrix serves as an evaluation criterion for the reliability of the position estimation model. The parameter selection process finalized when the image recognition rate for position estimation is more than 95%. The image recognition rate refers to the proportion of correctly classified samples in the total test samples. The SVM model used in this article achieved an image recognition rate of 95.41%.

IV. Experiment Evaluation

A. Introduction of Testbench

To confirm the effectiveness of the proposed position estimation method, our experiments were conducted using a Speedgoat as a real-time controller (sometimes referring as MBD rapid development), which acted as the controller prototype to execute our algorithm. This controller generates PWM signals into a real three-phase inverter, which drives an actual motor. The proposed initial rotor position estimation method was also tested on an SPMSM with low saliency, and its parameters are provided in Table II. The Speedgoat is a real-time target controller that can operate at a frequency of up to 150 MHz and has the capability to sample a 4-channel 16-bit A/D converter simultaneously on the used board. The PWM VSI was built using MOSFET Ipd082n10n3g and a three-phase half-bridge driver IR2110strpbf. The experimental platform is illustrated in Fig. 12. In order to verify the proposed estimation method, experiments have been conducted on a Speedgoat. The initial rotor position estimation scheme has been investigated using experiments on an SPMSM, and its parameters are listed in Table III. The Speedgoat is a real-time target controller whose

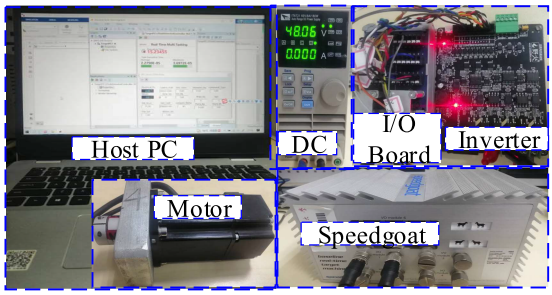

Fig. 12. Experimental platform.

TABLE III
SPECIFICATIONS OF THE MACHINE AND THE INJECTION SIGNAL

Items	Unit	Value
Output power	W	150
Rated current	A	2.5
Rated Voltage	V	48
Pole pairs	-	4
Resistance	mΩ	165
Inductance of d axis	μH	305
Inductance of q axis	μH	320
Rotor magnet flux linkage	$\text{mV} \cdot s$	15
Injected Signal Frequency	Hz	500
Injected Signal Amplitude	V	4

frequency can reach 150 MHz and is the ability to sample a 4-channel 16-bit A/D converter in a used board simultaneously. The PWM VSI is constructed by MOSFET Ipd082n10n3g and three-phase half-bridge driver IR2110strpbf. The experimental platform is shown in Fig. 12.

Generally, a larger amplitude of the HF voltage results in improved accuracy estimates of the position but can also generate losses, noise, and vibration. As the estimation process for initial position is short, the losses and noise from higher amplitude HFI can be neglected. Therefore, the amplitude of HFI can be selected to generate saturation saliency that ensures position estimation accuracy. Moreover, the carrier frequency of the HF signal injected should be far from the fundamental machine operating frequency so that the frequency current is easily separated. If the carrier frequency is excessively high, it can lead to insufficient HF amplitude current and increased disturbance due to the switching frequency. To trade-off, this article selects an HF voltage signal with a magnitude of 4 V and a frequency of 500 Hz, which is then injected into the stationary reference frame. Experiments are conducted with current sampling and PWM switch frequencies set at 20 and 20 kHz, respectively.

B. Saliency of the Test Machine

The saliency ratio is a value that can demonstrate the characteristic of saliency for a machine. However, due to its structurally symmetrical design, the SPMSM has little or no saliency. The saliency for the SPMSM depends on spatial saturation. Based on the electromagnetic saturation model, the saliency ratio is

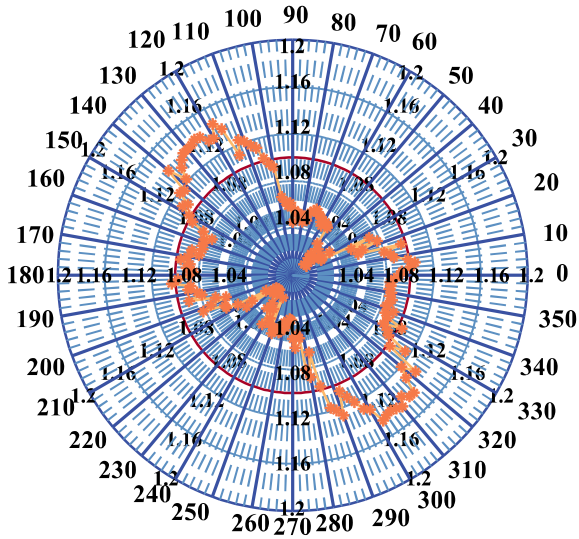

Fig. 13. Values of the saliency.

determined as

$$\xi = \frac{I_p + I_n}{I_p - I_n}. \tag{11}$$

Fig. 13 displays the values of the saliency ratio at various positions. As can be observed, the values of the saliency ratio are significantly different at different positions, as indicated by the orange–brown asterisk. At some positions, the saliency ratio is less than 1.04, and the maximum value of the saliency ratio in the experimental positions is not greater than 1.16. Because of its low saliency, the conventional observer-based position estimation performance is unsatisfactory.

To evaluate the performance of the estimated position over a 360° period, the error between the actual position and estimation position is defined as follows:

$$\Delta\theta_e = \begin{cases} \left|\hat{\theta}_e - \theta_e\right|, & \left|\hat{\theta}_e - \theta_e\right| <= 180^\circ \\ 360^\circ - \left|\hat{\theta}_e - \theta_e\right|, & \left|\hat{\theta}_e - \theta_e\right| > 180^\circ. \end{cases} \tag{12}$$

C. Estimation Performance Using Position Observer

To demonstrate the estimation performance of the observer, the experiment was implemented at a standstill with the injection angle at $\theta_e = 290^0$, as depicted in Fig. 14. The first subfigure from the top displays the real and imaginary part of the negative sequence current i_{c_n1} obtained by the investigation based on the conventional observer. The second and third subfigure presents the extracted position error ε_{pos} and pole information ε_{pol} using the conventional method, respectively. Meanwhile, the fourth subfigure demonstrates the actual position θ_e, the estimated positions $\hat{\theta}_e$, and the position estimation error $\Delta\theta_e$. Theoretically, the error signal ε_{pos} extracted through heterodyne method is converging near 0, which serves as an indicator that the estimated position is congruent with the actual position. However, as shown in the second and fourth subfigures of Fig. 14, the extracted position error ε_{pos} almost approaches 0, the estimated position is approximately 20 electrical degrees at

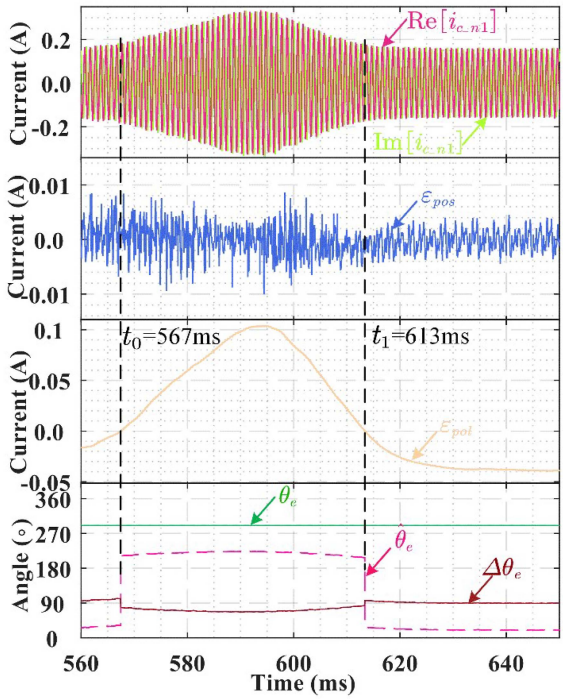

Fig. 14. Position estimation performance of the conventional observer at a standstill with the injection angle at 290°.

$\theta_e = 290^0$. Regrettably, the position estimation error $\Delta\theta_e$ is also nearly 90 electrical degrees, indicating an improper estimation result. It is important to note that, as depicted in the first subfigure of Fig. 14, interference signals occurring between t_0 and $t_1$can result in errors when extracting polarity information. Furthermore, as seen in the fourth subfigure of Fig. 14, such interference signals can also lead to significant deviations in estimation accuracy. Hence, conventional observers do not have the ability to eliminate interference signals, which can lead to large estimation errors when the HF rotating signal is disturbed.

Considering the polarity detection and more convenient, the estimated calculated position error is according to (12) and converted it into a display within an angle period of 180°. As shown in Fig. 15, the errors of the estimated position using the conventional observer are denoted by the brown asterisk. Only a few position errors fall within the blue circle with an error of less than 30°. However, many position errors exceed 90°, which is outside the red circle.

D. Estimation Performance Using Image Tracking

To operate the SPMSM test machine, a rotating vector is injected in the stationary reference frame at several positions. The images of the rebuilt current vector are different under various rotor positions, and the responded current appears in the form of different current trajectories in a plane. Based on the characteristics of these different current responses, corresponding position information can be extracted from the current image.

1) Estimation Position at Standstill: As shown in Fig. 16, the results of the injection angles at $\theta_e = 0^0$ without load are

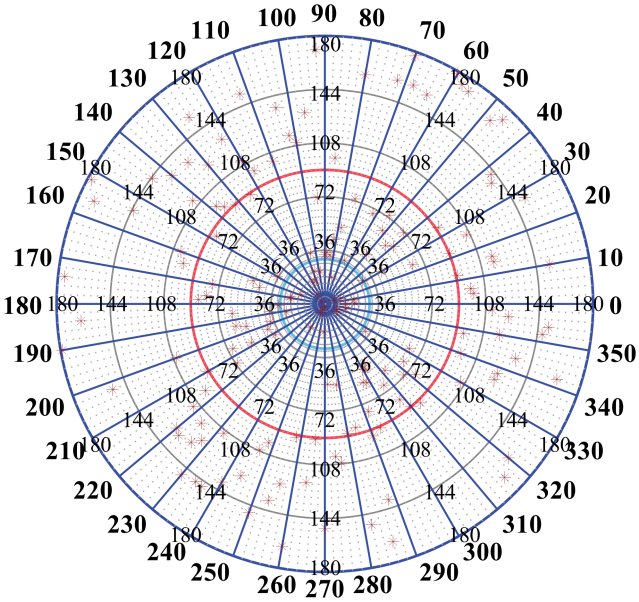

Fig. 15. Errors of estimated position using the conventional observer.

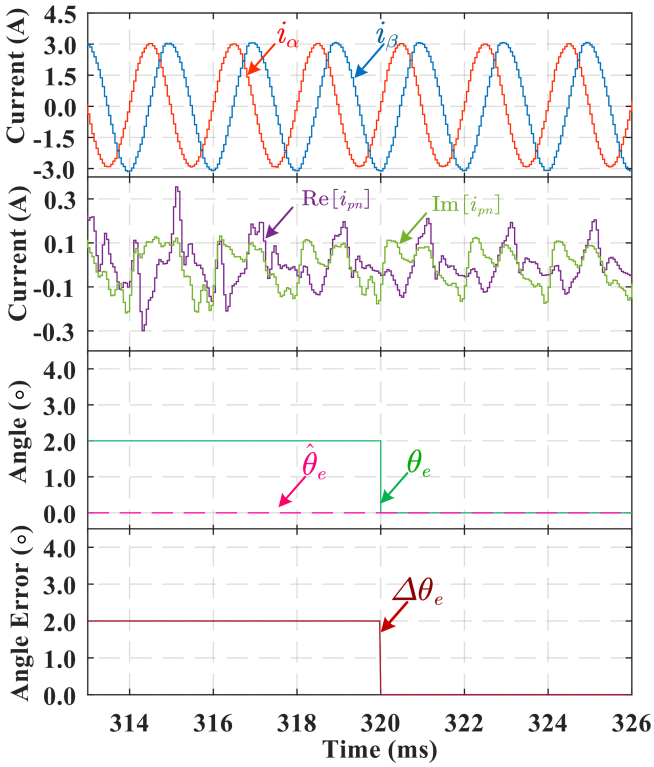

Fig. 16. Experimental results and position estimation performance without load at 0°.

presented. The i_α and i_β are displayed in the first subfigure, while the real part of composite current i_{pn} and the imaginary part of composite current i_{pn} are shown in the second subfigure. Actual position and estimated position are presented in the third subfigure, while the position estimation error $\Delta\theta_e$ is shown in the fourth subfigure. The descriptions of the subfigures in the following figures are the same. From the first subfigure, it is evident that the amplitude of $i_\alpha$and i_β is not equal, indicating

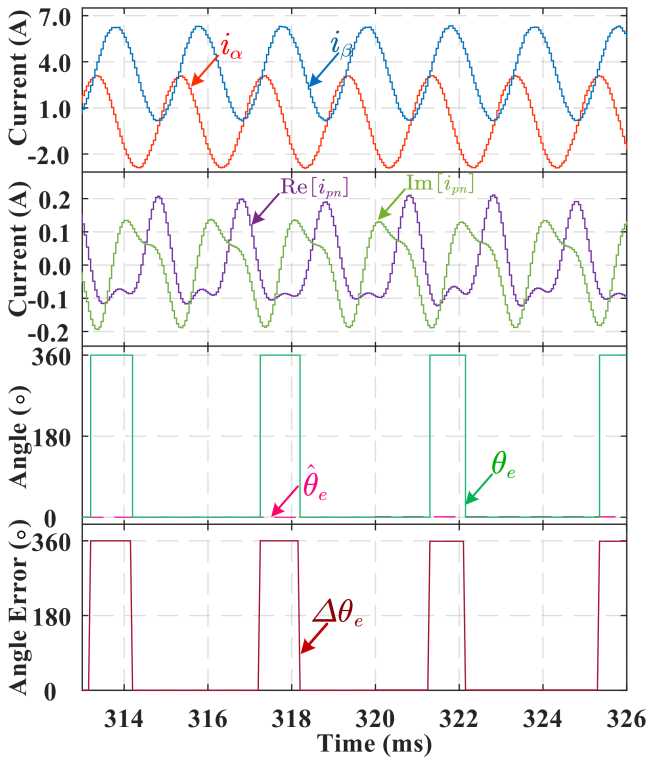

Fig. 17. Experimental results and position estimation performance with full load at 0°.

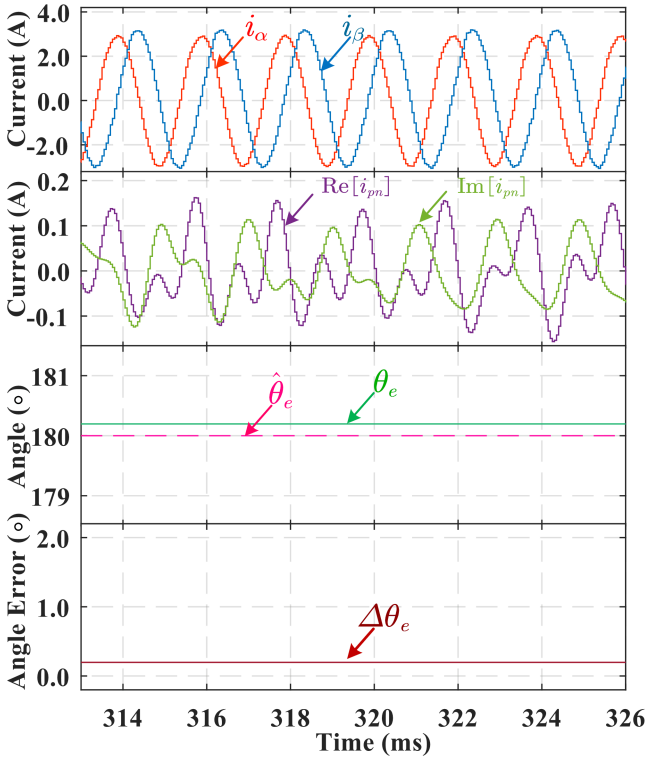

Fig. 18. Experimental results and position estimation performance without load at 180°.

that the stationary current contains negative-sequence current, which contains position information. In the second subfigure, $\mathrm{Re}[i_{pn}]$and $\mathrm{Im}[i_{pn}]$ show harmonic content. The amplitude, phase, and offset values of $\mathrm{Re}[i_{pn}]$ and $\mathrm{Im}[i_{pn}]$ also differ. As seen from the third and fourth subfigures, the position estimation performance is satisfactory, with a maximum $\Delta\theta_e$ of two electrical degrees.

To illustrate the impact of cross-saturation effects, the second experiment shows the results of the injection angles at full load in Fig. 17. It can be observed that the amplitude of the real and imaginary parts of i_{pn} is greater than in the absence of load, since saturation saliency increases with load. Under full load, $\Delta\theta_e$ is almost equal to 0 (360) electrical degree in the fourth subfigure.

2) Estimation Position With Interferences: To analyze the polarity information in the composite current vector, the results of the injection angles at no-load are displayed in Fig. 18. This is due to the substantial differences in amplitude and phase of the composite current harmonic displayed in the second subfigure, compared to the current shape shown in Fig. 16. As a result, the rotor position with polarity information can be directly obtained.

It is noted that during the initialization process of image recognition, which lasts from 0 to 60 ms, the estimated position output remains constant at the set value of 0 until the completion of the initialization process. As shown in Fig. 19, in the time range of 100 to 140 ms, the extracted HF current is confused with some interference signals, which subsequently leads to a negative-sequence current and rebuilt current distortion. When

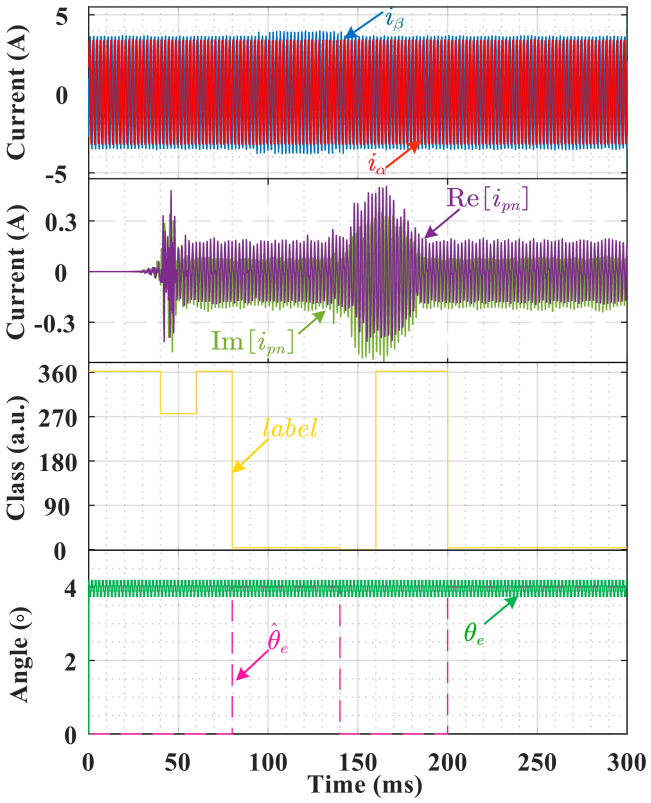

Fig. 19. Experimental position estimation result with interferences at 4°.

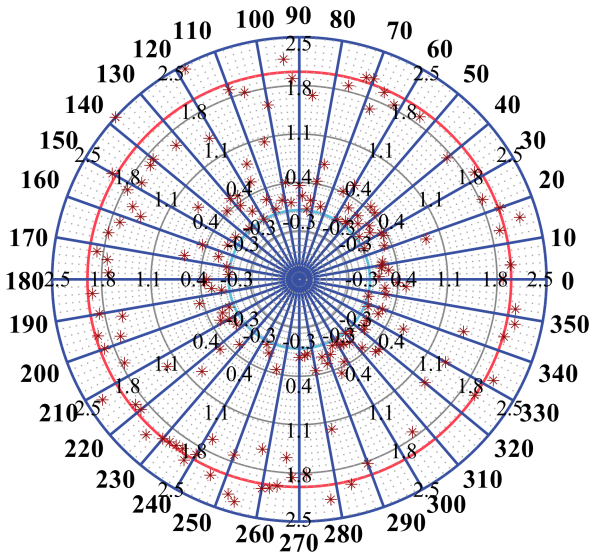

Fig. 20. Errors of estimated position using image tracking.

the method based on the image recognition algorithm accurately identified the interference signal, the categorization label value is 362. When there are signal interferences, the estimated position remains the same as the previous estimate in the program. The results of position estimation with signal interference are shown in Fig. 19. It should be noted that during the initialization process of image recognition, which lasts from 0 to 60 ms, the estimated position output remains constant at the set value of 0 until the completion of the initialization process.

3) Errors of Estimated Position Using Image Tracking: In order to evaluate the accuracy of the proposed method, the estimation error results for 180 test cases with 2° intervals between each test, covering the range of 0°–358°, are shown in Fig. 20. The values of position error are indicated by the brown asterisks. All of the position errors fall within the outermost circle in Fig. 20, with an error of less than 2.5°. As depicted in Fig. 20, the red circle represents the error range of 2°, and the majority of the position errors during the 180 tests are contained within this circle. These results indicate that the initial position estimation based on image tracking has a high level of precision.

4) Estimation Position at a Relatively Low Speed: To evaluate the dynamic performance of our proposed method, the experiments at 3 rpm without load is displayed in Fig. 21. The experimental results indicate that even in the presence of interference signals, our dynamic location estimation can achieve better estimation accuracy. The overall average error was 4.47°, and the maximum estimation error did not exceed 20°, except for the program initialization error.

5) Estimation Position Under the Change Load Condition: To evaluate the position estimation performance during start-up with a load, experiments were conducted from standstill with load to 2 rpm, as illustrated in Fig. 22. During this experiment, the motor began from a standstill state and gradually increased to 2 rpm under load until the load was unexpectedly unloaded around the 13 s. Our experimental results indicate that, overall,

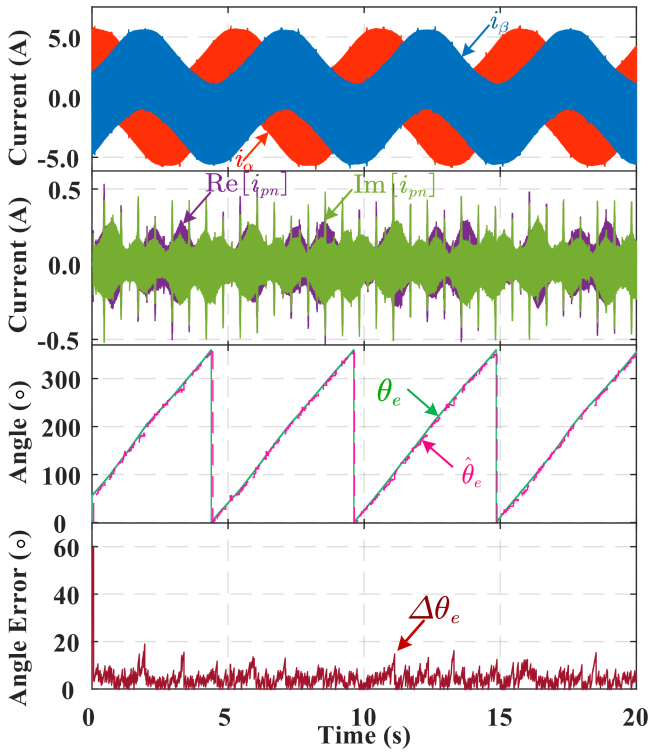

Fig. 21. Experimental result and position estimation performance at 3 rpm without load.

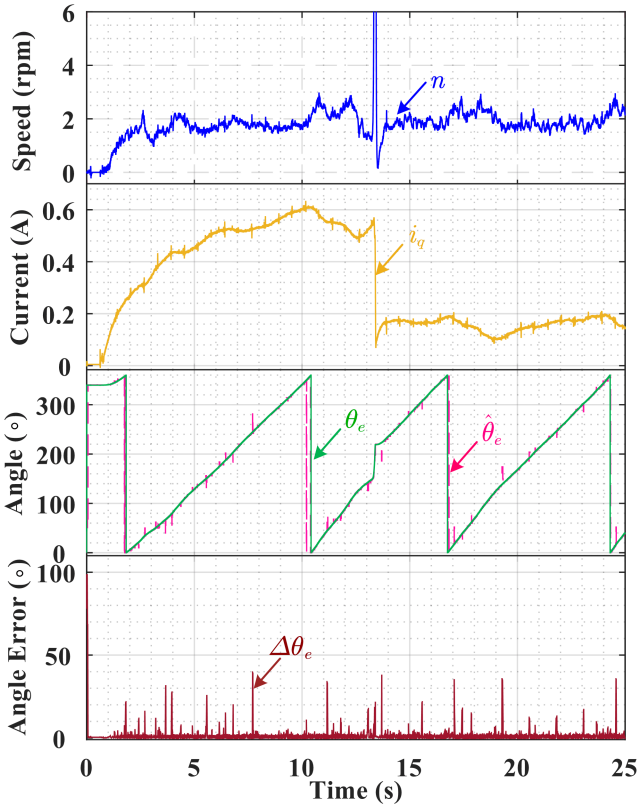

Fig. 22. Experimental result and position estimation performance of start-up with load.

the average error during the entire operation was 1.55°, excluding the partial position error resulting from fluctuations in the q-axis current during velocity modulation. These findings suggest that our proposed image tracking method delivers reliable performance for position estimation.

V. Conclusion

This article proposes an image-tracking-based method to obtain the initial position of electric machines with low saliency in order to improve the sensorless control performance of SPMSM. The proposed method utilizes a current vector image constructed from the negative and second harmonic components of the positive sequence of HF current signals in the stationary reference, which contains rich position information.

Compared to traditional HF rotating injection methods, existing saliency-based observers result in relatively large errors due to the effect of multiple saliencies and cross-saturation when used for motors with low saliency ratios. To address this issue, the proposed method considers cross-saturation and interference signals to effectively identify subtle position features and enable accurate sensorless control of SPMSM with very low saliency ratios.

The experimental findings demonstrate that our proposed method exhibits high estimation accuracy and robustness even under changing load conditions. In static conditions, the position error is less than 2.5 electrical degrees. At low speeds, the average dynamic estimated position error is less than 4.5 electrical degrees, even in constantly changing working conditions. It is noteworthy that while the experimental results presented were obtained using an SPMSM with a low saliency ratio, the proposed method can be applied to other PMSMs as well.

References

[1] Z. Chen, M. Tomita, S. Doki, and S. Okuma, "An extended electromotive force model for sensorless control of interior permanent-magnet synchronous motors," *IEEE Trans. Ind. Electron.*, vol. 50, no. 2, pp. 288–295, Apr. 2003.

[2] C. De Angelo, G. Bossio, J. Solsona, G. O. Garcia, and M. I. Valla, "Mechanical sensorless speed control of permanent-magnet AC motors driving an unknown load," *IEEE Trans. Ind. Electron.*, vol. 53, no. 2, pp. 406–414, Apr. 2006.

[3] J. Solsona, M. I. Valla, and C. Muravchik, "On speed and rotor position estimation in permanent-magnet AC drives," *IEEE Trans. Ind. Electron.*, vol. 47, no. 5, pp. 1176–1180, Oct. 2000.

[4] H. W. De Kock, M. J. Kamper, and R. M. Kennel, "Anisotropy comparison of reluctance and PM synchronous machines for position sensorless control using HF carrier injection," *IEEE Trans. Power Electron.*, vol. 24, no. 8, pp. 1905–1913, Aug. 2009.

[5] Z. Mai et al., "HF pulsating carrier voltage injection method based on improved position error signal extraction strategy for PMSM position sensorless control," *IEEE Trans. Power Electron.*, vol. 36, no. 8, pp. 9348–9360, Aug. 2021.

[6] B. Han, Y. Shi, X. Song, K. Hong, and K. Mao, "Initial rotor position detection method of SPMSM based on new high frequency voltage injection method," *IEEE Trans. Power Electron.*, vol. 34, no. 4, pp. 3553–3562, Apr. 2019.

[7] Y. Zhang, Z. Yin, C. Bai, G. Wang, and J. Liu, "A rotor position and speed estimation method using an improved linear extended state observer for IPMSM sensorless drives," *IEEE Trans. Power Electron.*, vol. 36, no. 12, pp. 14062–14073, Dec. 2021.

[8] H. Li, S. Zheng, and H. Ren, "Self-correction of commutation point for high-speed sensorless BLDC motor with low inductance and nonideal back EMF," *IEEE Trans. Power Electron.*, vol. 32, no. 1, pp. 642–651, Jan. 2017.

[9] H. Li, Z. Wang, C. Wen, and X. Wang, "Sensorless control of surface-mounted permanent magnet synchronous motor drives using nonlinear optimization," *IEEE Trans. Power Electron.*, vol. 34, no. 9, pp. 8930–8943, Sep. 2019.

[10] X. Song, J. Fang, B. Han, and S. Zheng, "Adaptive compensation method for high-speed surface PMSM sensorless drives of EMF-based position estimation error," *IEEE Trans. Power Electron.*, vol. 31, no. 2, pp. 1438–1449, Feb. 2016.

[11] P. L. Jansen and R. D. Lorenz, "Transducerless position and velocity estimation in induction and salient AC machines," *IEEE Trans. Ind. Appl.*, vol. 31, no. 2, pp. 240–247, Mar./Apr. 1995.

[12] H. Kim, K.-K. Huh, R. D. Lorenz, and T. M. Jahns, "A novel method for initial rotor position estimation for IPM synchronous machine drives," *IEEE Trans. Ind. Appl.*, vol. 40, no. 5, pp. 1369–1378, Sep./Oct. 2004.

[13] M. W. Degner and R. D. Lorenz, "Using multiple saliencies for the estimation of flux, position, and velocity in AC machines," *IEEE Trans. Ind. Appl.*, vol. 34, no. 5, pp. 1097–1104, Sep./Oct. 1998.

[14] J. Hu, J. Liu, and L. Xu, "Eddy current effects on rotor position estimation and magnetic pole identification of PMSM at zero and low speeds," *IEEE Trans. Power Electron.*, vol. 23, no. 5, pp. 2565–2575, Sep. 2008.

[15] Y.-S. Jeong, R. D. Lorenz, T. M. Jahns, and S.-K. Sul, "Initial rotor position estimation of an interior permanent-magnet synchronous machine using carrier-frequency injection methods," *IEEE Trans. Ind. Appl.*, vol. 41, no. 1, pp. 38–45, Jan./Feb. 2005.

[16] J. M. Kim, S. J. Kang, and S. K. Sul, "Vector control of interior permanent magnet synchronous motor without a shaft sensor," in *Proc. Appl. Power Electron. Conf.*, 1997, pp. 743–748.

[17] F. Briz, M. W. Degner, A. Diez, and R. D. Lorenz, "Measuring, modeling, and decoupling of saturation-induced saliencies in carrier-signal injection-based sensorless AC drives," *IEEE Trans. Ind. Appl.*, vol. 37, no. 5, pp. 1356–1364, Sep./Oct. 2001.

[18] H. Zhu, X. Xiao, and Y. D. Li, "A simplified high frequency injection method for PMSM sensorless control," in *Proc. IEEE 6th Int. Power Electron. Motion Control Conf.*, 2009, pp. 401–405.

[19] X. Zhang, H. Li, S. Yang, and M. Ma, "Improved initial rotor position estimation for PMSM drives based on HF pulsating voltage signal injection," *IEEE Trans. Ind. Electron.*, vol. 65, no. 6, pp. 4702–4713, Jun. 2018.

[20] J. H. Jang, S. K. Sul, and Y. C. Son, "Current measurement issues in sensorless control algorithm using high frequency signal injection method," in *Proc. 38th IAS Annu. Meeting Conf. Rec. Ind. Appl.*, 2003, vol. 2, pp. 1134–1141.

[21] J. I. Ha and S. K. Sul, "Physical understanding of high frequency injection method to sensorless drives of an induction machine," in *Proc. Conf. Rec. IEEE Ind. Appl. Conf. 35th IAS Annu. Meeting World Conf. Ind. Appl. Elect. Energy*, 2000, pp. 1802–1808.

[22] J. Cilia, G. M. Asher, K. J. Bradley, and M. Sumner, "Sensorless position detection for vector-controlled induction motor drives using an asymmetric outer-section cage," *IEEE Trans. Ind. Appl.*, vol. 33, no. 5, pp. 1162–1169, Sep./Oct. 1997.

[23] L. Shen, J. Wu, and S. Yang, "Initial position estimation in SRM using bootstrap circuit without predefined inductance parameters," *IEEE Trans. Power Electron.*, vol. 26, no. 9, pp. 2449–2456, Sep. 2011.

[24] X. Jin, R. Ni, W. Chen, F. Blaabjerg, and D. Xu, "High-frequency voltage-injection methods and observer design for initial position detection of permanent magnet synchronous machines," *IEEE Trans. Power Electron.*, vol. 33, no. 9, pp. 7971–7979, Sep. 2018.

[25] N. Bianchi, S. Bolognani, J.-H. Jang, and S.-K. Sul, "Comparison of PM motor structures and sensorless control techniques for zero-speed rotor position detection," *IEEE Trans. Power Electron.*, vol. 22, no. 6, pp. 2466–2475, Nov. 2007.

[26] B. Shuang and Z.-Q. Zhu, "A novel sensorless initial position estimation and startup method," *IEEE Trans. Ind. Electron.*, vol. 68, no. 4, pp. 2964–2975, Apr. 2021.

[27] D. Raca, P. Garcia, D. Dí. Reigosa, F. Briz, and R. D. Lorenz, "Carrier-signal selection for sensorless control of pm synchronous machines at zero and very low speeds," *IEEE Trans. Ind. Appl.*, vol. 46, no. 1, pp. 167–178, Jan. 2010.

[28] G. Bi, N. Zhao, G. Zhang, R. Jing, G. Wang, and D. Xu, "Current vector angle adaptive adjustment based rotor position offset error suppression method for sensorless PMSM drives," *IEEE Trans. Power Electron.*, vol. 36, no. 9, pp. 10536–10547, Sep. 2021.

[29] X. Fu, Y. Xu, H. He, and X. Fu, "Initial rotor position estimation by detecting vibration of permanent magnet synchronous machine," *IEEE Trans. Ind. Electron.*, vol. 68, no. 8, pp. 6595–6606, Aug. 2021.

[30] P. Xu and Z. Q. Zhu, "Initial rotor position estimation using zero-sequence carrier voltage for permanent-magnet synchronous machines," *IEEE Trans. Ind. Electron.*, vol. 64, no. 1, pp. 149–158, Jan. 2017.
[31] L. M. Gong and Z. Q. Zhu, "Robust initial rotor position estimation of permanent-magnet brushless AC machines with carrier-signal-injection-based sensorless control," *IEEE Trans. Ind. Appl.*, vol. 49, no. 6, pp. 2602–2609, Nov./Dec. 2013.
[32] T. S. Slininger, Y. Xu, and R. D. Lorenz, "Enhancing estimation accuracy by applying cross-correlation image tracking to self-sensing including evaluation on a low saliency ratio machine," in *Proc. IEEE Energy Convers. Congr. Expo.*, 2016, pp. 1–7.
[33] D. Liu, D. Niu, H. Wang, and L. Fan, "Short-term wind speed forecasting using wavelet transform and support vector machines optimized by genetic algorithm," *Renewable Energy*, vol. 62, pp. 592–597, Feb. 2014.
[34] Y. Wang, J. Wang, and X. Wei, "A hybrid wind speed forecasting model based on phase space reconstruction theory and Markov model: A case study of wind farms in northwest China," *Energy*, vol. 91, pp. 556–572, Nov. 2015.
[35] E. Vazquez-Sanchez, J. Gomez-Gil, J. C. Gamazo-Real, and J. F. Diez-Higuera, "A new method for sensorless estimation of the speed and position in brushed DC motors using support vector machines," *IEEE Trans. Ind. Electron.*, vol. 59, no. 3, pp. 1397–1408, Mar. 2012.
[36] R. Zhong et al., "Accurate model of switched reluctance motor based on indirect measurement method and least square support vector machine," *Int. Eng. Technol. Elect. Power Appl.*, vol. 10, no. 9, pp. 916–922, Nov. 2016.

Henghong Wang (Student Member, IEEE) received the B.Sc. degree in vehicles engineering from the Xihua University, Sichuan, China, in 2008, and the M.Sc. degree in vehicles engineering from the Hunan University, Hunan, China, in 2014. He is currently working toward the Ph.D. degree in electrical engineering with the Southeast University, Nanjing, China.

From 2008 to 2020, he was with the Guangxi Yuchai Machinery Company, LTD, China, as the new Energy Power Research and Development Control Engineer. His research interests include control of sensorless and design for permanent magnet machines for electric vehicles.

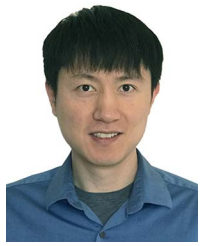

Jiyao Wang (Member, IEEE) received the B.S. degree from the Tsinghua University, Beijing, China, in 2010, and the Ph.D. degree from the University of Wisconsin-Madison, Madison, WI, USA, in 2015, both in electrical engineering.

From 2016 to 2020, he was with the Ford Motor Company, Dearborn, MI, USA, where he was a part of the Product Development team for the electric motor control and drive system of Ford and Lincoln brand production level electric vehicles including F150 Hybrid, Aviator Hybrid, and Mustang Mach-E. In 2021, he joined the Department of Electrical Engineering, Southeast University, Nanjing, China. His research interests include designs and controls for the integration of electric machine drive system.

Wei Xu (Member, IEEE) received the B.S. degree in mechanical engineering from the Tongji University, Shanghai, China, in 2004, the M.S. degree in mechanical engineering from the Leibniz University of Hannover, Hannover, Germany, in 2007, and the Ph.D. degree in mechanical engineering from the University of Wisconsin–Madison, Madison, WI, USA, in 2013.

From 2013 to 2019, he was with the Ford Motor Company, Dearborn, MI, USA, as a Motor Control Engineer and later as a Technical Expert. Since 2019, he has been a Faculty Member with the Department of Electrical Engineering, Southeast University, Nanjing, China. His research interests include design and control of electrical machines and drive system.